Materials and Design 191 (2020) 108643

Contents lists available at ScienceDirect

Materials and Design

journal homepage: www.elsevier.com/locate/matdes

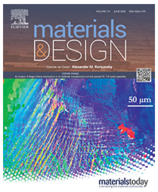

Hinges for origami-inspired structures by multimaterial additive manufacturing

Marius A. Wagner [a], Jian-Lin Huang [b], Philipp Okle [a], Jamie Paik [b], Ralph Spolenak [a,*]

[a] Laboratory for Nanometallurgy, Department of Materials, ETH Zürich, 8093 Zürich, Switzerland
[b] Reconfigurable Robotics Laboratory, EPFL, MED11326, Station 9, 1015 Lausanne, Switzerland

HIGHLIGHTS

- Comparison of three different additive-manufacturing-based flexural hinges
- Investigation of the impact of the design parameters on load carrying capability and flexural properties
- Discussion of the 3D-printed hinge fatigue properties and constituting mechanisms
- Guideline for the material and design parameter selection for optimizing the required hinge's mechanical properties

GRAPHICAL ABSTRACT

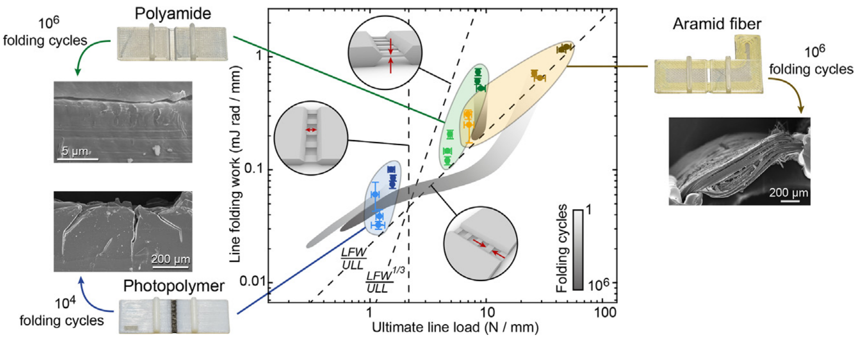

ARTICLE INFO

Article history:
Received 8 December 2019
Received in revised form 9 February 2020
Accepted 12 March 2020
Available online 13 March 2020

Keywords:
Flexural hinges
3D printing
Origami
Fatigue
Folding joints
Multimaterial additive manufacturing

ABSTRACT

Recent studies demonstrate novel metamaterials featuring unique properties by combining origami-inspired designs with additive manufacturing. In particular, the use of flexural hinges endows distinct advantages towards miniaturization and fabrication; however, there are limited applications due to the limited loading and fatigue resistance of the hinges. In this study, we focus on testing and characterizing mechanical properties of flexural hinges so that our findings could have immediate applications in 3D-printed origami structures. We introduce an *aramid* fiber composite hinge and compare it to a single-material polyamide and a multimaterial photopolymer hinge. We investigate the impact of the materials and geometric design parameters on the load carrying capability and flexural properties. Furthermore, the fatigue behavior of the hinges is characterized, identifying the constitutive mechanisms. We consolidate all the data and findings to construct a comprehensive *design parameter – property map*, which serves as a guideline for optimizing hinge performance for a given set of required properties.

© 2020 The Authors. Published by Elsevier Ltd. This is an open access article under the CC BY-NC-ND license (http://creativecommons.org/licenses/by-nc-nd/4.0/).

1. Introduction

Folding is one of the most fundamental mechanisms found in nature at various length scales. At a molecular level, folding is responsible for the self-assembly of proteins and the packaging of DNA [1]. At a cellular level, it allows the formation of various organs [1]. Up to the macroscopic level, where the folding facilitates the storage of insect wings at rest [2]. In the traditional art form of origami, a single sheet of paper can be folded to create a variety of different complex shapes. Origami designs embody various unique advantages including a simplified manufacturing process, programmable reconfigurations, and high

---

* Corresponding author.
E-mail address: ralph.spolenak@mat.ethz.ch (R. Spolenak).

https://doi.org/10.1016/j.matdes.2020.108643
0264-1275/© 2020 The Authors. Published by Elsevier Ltd. This is an open access article under the CC BY-NC-ND license (http://creativecommons.org/licenses/by-nc-nd/4.0/).

volumetric changes between the resting state and the desired shape. Therefore, origami has found engineering applications in fields like aero-space, medicine and automotive industry and is intensively researched [3]. In space, they have proven to be useful for foldable sunshields and solar sails [3,4]. Based on origami, novel metamaterials and structures demonstrate interesting shape changing capabilities based on folding [5,6], negative Poisson's ratio [7], bi-stability [8,9], tunable coefficient of thermal expansion [10], and switchable mechanical properties [11]. Another application is in the field of origami-inspired soft robots [12–15]. In contrast to their industrial counterparts, origami robots can fold into multiple shapes allowing them to reconfigure and adapt to their environment, therefore, they can serve multiple purposes [12,13].

While origami traditionally fold at creases in a thin sheet, the novel engineered structures use hinges as their central mechanical component. Hinges facilitate the controllable deformation in a localized defined region. The desired properties of a hinge depend strongly on the application. There are two fundamental approaches in designing a hinge. A pin joint provide a single rotational degree of freedom (DoF) with a cylindrical stud that connects two links. Thus, the links can pivot freely about the central axis of the stud [16]. The advantage of these hinges is the low resistance to folding and their precisely defined rotational axis. On the downside, pin joints suffer from wear, and require assembly and maintenance [17]. An alternative to a mechanical pin joint is a compliant mechanism such as a flexural hinge. Flexural hinges consist of a small length flexible segment connecting two rigid members. The motion is achieved by strain in the flexible segment. In a flexural hinge, the wear can be significantly reduced. They are easier to miniaturize, cheaper to fabricate, more reliable, and requiring no assembly [17]. However, depending on the design, the center of rotation may not be stable and induce uncontrolled parasitic DoFs [18]. Due to the localized strain, fatigue is a crucial aspect, which needs to be considered when designing flexure joints. Most of the research in the field of origami-inspired structures relies on flexural hinges, due to the advantages discussed above.

Additive manufacturing (AM) technologies can often overcome manufacturing challenges of complex structures, which have assembly and joining constraints. This makes AM a uniquely suited technology for the fabrication of origami-inspired structures. A variety of studies have shown that AM can be used to fabricate origami-inspired structures with properties hitherto not observed (shape changing capability [5], tunable bi-stability [9], or deployable robotic systems [15]). However, it is rare to have these structures finding their way into real life applications. This disparity is mainly due to the low load carrying capability and fatigue resistance of the folding joints: these two main obstacles need to be overcome in order to bring origami structures closer to applications.

The research on 3D-printed flexural hinges is scarce. It is known that specific cutout patterns in the hinge can prescribe motions [18]. In a recent study, a 3D-printed flexural hinge was simulated using finite element analysis and compared to a non-linear beam model [19]. Others use an analytical model composed of a rotational and a tension spring to model the behavior of hinges fabricated by fused deposition modeling (FDM) [8]. Gibson et al. [20] reviewed the suitability of different AM polymers for application in hinges. Polyethylene, polypropylene, and polyamide showed the most promising properties. Furthermore, the flexural behavior of photopolymer hinges fabricated on an inkjet 3D printer was examined experimentally. In that study, the blocked force was measured for different hinge thicknesses, and the experimental results were compared to the finite element simulations.

While AM is prevalent in various structural manufacturing and research efforts in their new application fields, to date, there is no research describing the load carrying capability and fatigue properties of hinges manufactured by AM. In this work, we perform an in-depth investigation of these disregarded but essential aspects. Three classes of hinges fabricated by different AM processes are characterized experimentally (Fig. 1). The relation between mechanical properties and design parameters is studied. Further, the fatigue mechanisms in the different hinge classes are examined.

The concept of an aramid composite hinge is introduced and compared to two existing hinge classes, i.e. a single-material polyamide (PA) and a multimaterial photopolymer hinge. This allows a benchmark of the mechanical properties.

2. Methods

2.1. Materials, design and fabrication

2.1.1. Aramid hinge

The aramid hinge consists of two rigid polyamide segments, which are connected in the hinge region by bundles of continuous aramid fibers impregnated by a polyamide matrix (Fig. 1a). The hinges are fabricated from the commercial materials “tough nylon” and continuous aramid fiber filaments (Markforged Ltd.) [21]. Carbon and glass fiber composite filaments show fracture in the first folding cycles, proving to be unsuitable for the applications in hinges. Both the aramid and the PA hinges are fabricated on a Markforged Mark Two fused deposition modeling (FDM) 3D printer.

2.1.2. Polyamide hinge

The single material polyamide (PA) hinge is printed by FDM of the commercial PA6 (“tough Nylon” Markforged Ltd. [22]) (Fig. 1b). The flexible hinge region is designed as a sheet with a reduced thickness, shifted to the bottom of the rigid segment. This allows printing the hinge without support structures, which results in improved mechanical properties. To maximize the strength of the hinges, the long axis is aligned with the direction of the print head movement. In the FDM printing process, a nozzle with a 0.4 mm diameter is used. The layer height is 0.1 mm for the hinges with the thickness of 0.1 mm and 0.2 mm for the ones with a hinge thickness of 0.2 mm.

2.1.3. Photopolymer hinge

The photopolymer hinges are fabricated on a Stratasys Connex3 Objet500 inkjet 3D printer (Fig. 1c). The rigid segments of the hinge are made from a UV curable rigid thermoset (VeroWhitePlus Stratasys Ltd. [23]) and the flexural hinge consists of the flexible thermoset (Agilus30 Stratasys Ltd. [24]). Small gaps are introduced in the hinge region, to reduce the concentration of stresses. Upon bending, the material on the compression side expands laterally and contracts on the tension side, due to the Poisson effect. This introduces stress concentrations, which accumulate along the hinge width. To reduce these stress concentrations, cutouts are introduced into the flexible materials, which prevent the accumulation of lateral strains and stresses.

To minimize the effect of variations in UV dosage in the Connex process, all photopolymer specimens are printed with the matte surface finish option, encapsulated in a shell of hydrogel support material (SUP706 Stratasys Ltd. [25]) [26]. After printing, the support material is removed mechanically and the specimens are stored in a dark environment to avoid post curing. To minimize the influence of ageing, the time between printing and testing is kept as constant as possible throughout all experiments. The detailed hinge geometries and the values of the design parameters for the respective hinge classes are in the Supporting Information (SI).

2.2. Experimental characterization

2.2.1. Tensile properties

The load carrying capability of the hinges is described in terms of the ultimate line load (*ULL*), which is defined as the maximum load divided by the width of the hinge (N mm^{-1}). By normalization with the width one receives a measure of the structural strength, allowing the comparison of different designs and materials [27]. The *ULL* is characterized

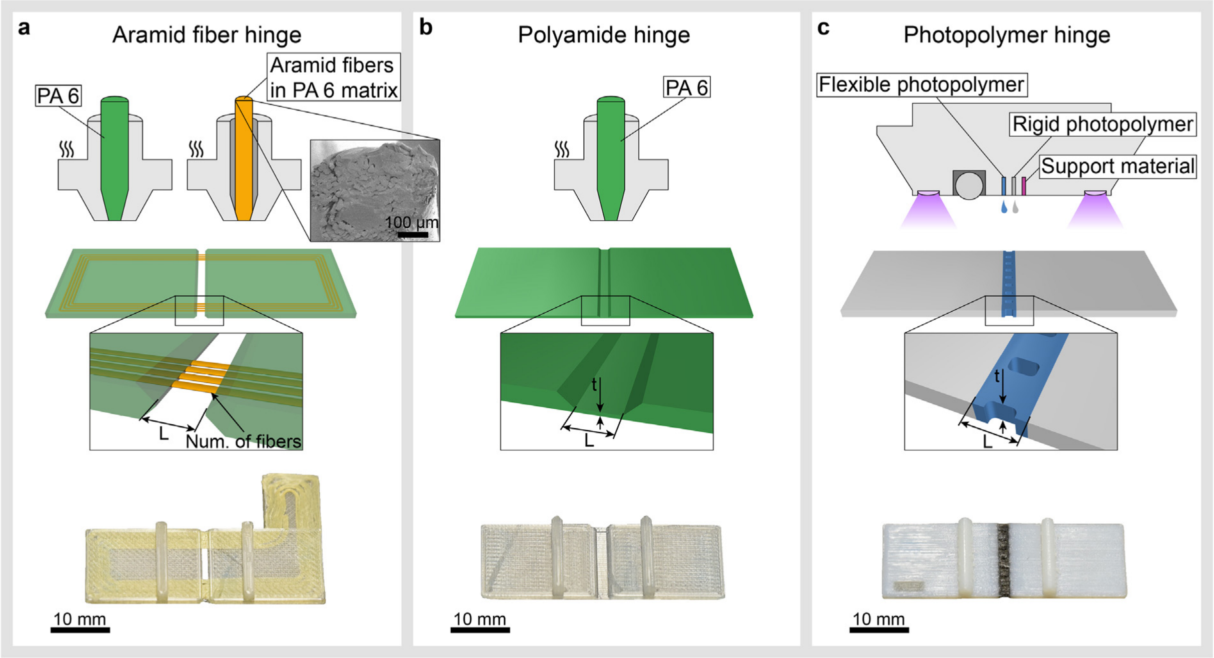

Fig. 1. Three classes of 3D printed hinges investigated, processes and design parameters. (a) Aramid hinge, (b) PA hinge and (c) photopolymer hinge. The top row illustrates the respective manufacturing technologies, (a) multimaterial FDM, (b) single-material FDM and (c) multimaterial inkjet. The middle row indicates the design parameters varied, hinge length and number of fiber bundles (a) and hinge thickness (b, c). The bottom row shows images of the 3D-printed specimens. The ridge on the top side of the hinge is added to facilitate accurate repeatable positioning in the experimental investigation. Note that the hinge region of the PA hinge (b) is shifted to the bottom. Thus, it can be fabricated without requiring support material, which improves the mechanical properties.

depending on the design parameters and the number of folding cycles. Tensile tests are performed on an Instron E3000 universal testing machine equipped with a 5 kN load cell, at a controlled strain rate of 1 s^{-1}. The photopolymers of the Connex 3D printer are highly viscoelastic and thus rate dependent [28]. While this dependence is outside of the scope of this study, brief data of the impact of strain rate on the load carrying capability of photopolymer hinges are in the SI.

2.2.2. Flexural properties

The flexural properties of the hinges are measured using a custom-built setup, consisting of a motor, a rotating wing, and a stationary load cell (see SI). One side of the hinge is fixed to the moving wing, while the other side is pushed against the load cell. Zhakypov et al. [29] provides a more detailed description of the setup. The maximum folding angle of 160° and an angular velocity of 5°/s are selected. All hinges are folded towards the side, which faced the print bed during fabrication. The bending moment is calculated from the normal force and the distance from the center of rotation to the contact point on the load cell. For each set of parameters, we test three specimens. Since the different hinges show non-linear behavior in the characteristic bending moment – folding angle curves, the definition and comparison of the bending stiffness is difficult. Therefore, the area under the loading curve, representing the work required for folding, is used as comparable measure. Similar to the load carrying capability, the folding work is normalized by dividing through the hinge width, which yields the line folding work (*LFW*) (mJ rad mm^{-1}).

2.2.3. Fatigue

The influence of fatigue on the tensile and flexural properties is characterized by performing the experiments as described above, after subjecting the specimen to a certain number of folding cycles. One cycle consists of folding the hinge from flat as-printed state, to the maximum folded state (folding angle 180°) and back. This corresponds to a strain-controlled fatigue with an R-ratio of zero, as long as the material behaves elastically. Since the polymers investigated exceed the limit of elastic strain and exhibit viscoelastic properties, stress with the opposite sign (tension on the compression side and vice versa) is generated in the unloading step. This results in $-1 < R < 0$. Fatigue is highly sensitive to the amplitude of stress and strain. The nominal strain amplitude in the material at complete folding varies greatly between the hinge classes and depends on the design parameters. In the fatigue specimens, the nominal strain amplitude amounts to 31% for the aramid and PA hinge and 87% for the photopolymer hinge. In particular, the strain in the aramid hinges deviates from this theoretical value, which will be discussed later. We selected the design parameters for the fatigue specimens, such that the strain amplitude is maximized for the investigated range (see SI). Therefore, the presented data can be regarded as the most severe case of fatigue. Up to 200 cycles specimens are folded manually. A Hydropuls fatigue-testing machine (Instron structural testing systems) is used to achieve higher numbers of folding cycles, at a frequency of 10 Hz. In the fatigue study, five specimens are tested for each respective set of folding cycles.

A sole description of the flexural fatigue by measuring the reduction of *LFW* with increasing numbers of folding cycles is not sufficient, since it is impossible to differentiate between the distinct phenomenological mechanisms leading to the decrease in *LFW*. A reduction in *LFW* results either from the accumulation of plastic deformation leading to a decrease in the effective angle of folding in the experiment (defined as 160° maximum folding angle of the setup minus the residual angle of the hinge), or reduction in stiffness of the hinge itself. Examining the folding work versus the residual angle allows to determine whether the residual angle or a stiffness decreasing mechanism is prevalent for the reduction in *LFW*. The black solid lines in Fig. 2i describe how the *LFW* would decrease due to increasing residual angle for a material that exhibits a cyclic stable stiffness. For sake of simplicity, the stiffness curves are approximated as linear, quadratic (progressive) and square root (degressive). The normalized *LFW* as a function of the effective folding angle can be calculated as:

$$LFW_l = n_l \int_0^{\alpha_{eff}} x \, dx \tag{1a}$$

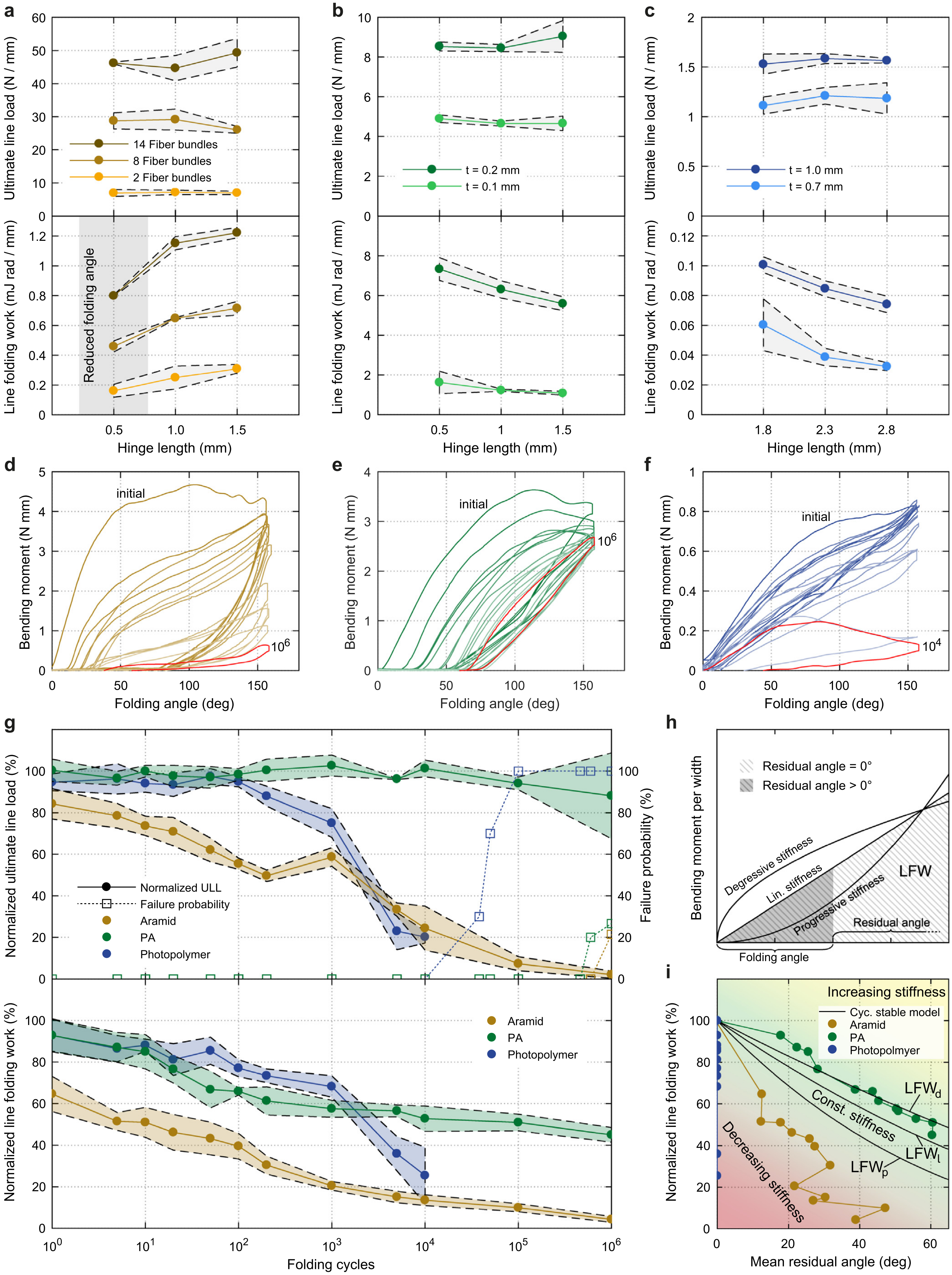
a
Ultimate line load (N / mm)
14 Fiber bundles
8 Fiber bundles
2 Fiber bundles
Line folding work (mJ rad / mm)
Reduced folding angle
Hinge length (mm)
0.5
1.0
1.5
b
t = 0.2 mm
t = 0.1 mm
Hinge length (mm)
c
t = 1.0 mm
t = 0.7 mm
1.8
2.3
2.8
Hinge length (mm)
d
Bending moment (N mm)
initial
10^6
Folding angle (deg)
e
initial
10^6
Folding angle (deg)
f
initial
10^4
Folding angle (deg)
g
Normalized ultimate line load (%)
Failure probability (%)
Normalized ULL
Failure probability
Aramid
PA
Photopolymer
Normalized line folding work (%)
Folding cycles
10^0
10^1
10^2
10^3
10^4
10^5
10^6
h
Bending moment per width
Residual angle = 0°
Residual angle > 0°
Degressive stiffness
Lin. stiffness
Progressive stiffness
LFW
Residual angle
Folding angle
i
Normalized line folding work (%)
Increasing stiffness
Cyc. stable model
Aramid
PA
Photopolmyer
LFW_d
Const. stiffness
LFW_l
LFW_p
Decreasing stiffness
Mean residual angle (deg)

$$LFW_p = n_p \int_0^{\alpha_{eff}} x^2 \, dx \tag{1b}$$

$$LFW_d = n_d \int_0^{\alpha_{eff}} \sqrt{x} \, dx \tag{1c}$$

with $\alpha_{eff} = 160^\circ - \alpha_{residual}$ and n being normalization factors, such that $LFW_l(160) = LFW_p(160) = LFW_d(160) = 1$. The introduction of n allows the comparison of the *LFW* for the different curve shapes. The theoretical model is illustrated in Fig. 2h. The stiffness of the hinge remains constant and the area under the loading curve (i.e. the *LFW*) is only reduced by a change in the folding angle. Depending on the shape of the moment – angle curve, the decrease in *LFW* due to the residual angle changes. A material can deviate from this either by cyclic decrease in stiffness (red region) or by a cyclic stiffness increase related to a hardening effect (yellow region), as shown in Fig. 2i. If the reduction in *LFW* from the experiments appears below the theoretical model, this is a sufficient condition to identify a stiffness decrease. On the other hand, for a stable stiffness it is necessary to have the hinge data in this cyclic stable regime. Since the exact shape of the moment – angle curve is only roughly approximated in the model, a slight reduction in stiffness could be present, even if the data lies inside the cyclic stable region. Further clarification can be achieved by examining the hysteresis loops for increasing numbers of folding.

Evidence for fatigue is investigated using scanning electron microscopy (SEM). The micrographs are taken on a JSM-7100F JEOL SEM, using the secondary electron contrast to investigate the surface topography.

3. Results

The tested ultimate line load (*ULL*) based on the design parameters is shown in Fig. 2a – c top row. The solid points represent the mean of three experiments and the dashed line shows the standard deviation. Unsurprisingly, the *ULL* of the aramid fiber hinge largely depends on the amount of fiber bundles, which are placed across the hinge. The same holds true for the thickness of the hinge region for polyamide (PA) hinges and photopolymer hinges. The hinge length is found to not significantly affect the *ULL* for all three materials in the range investigated.

The line folding work (*LFW*) depending on the design parameters is shown in Fig. 2a – c (bottom row). The number of fibers and the thickness of the hinge, have a large influence on the *LFW*. The aramid hinges with a length of 0.5 mm cannot be folded up to an angle of 160°, as the rigid segments collide (Fig. 2a bottom). Therefore, the folding angle in the experiment is reduced from 160° to 120°. For this reason, the *LFW* is not comparable and these data points are excluded from the discussion. The PA and the photopolymer hinges show a decrease in *LFW* for an increase in hinge width. For the aramid hinges, the opposite relation is found, an increase in hinge length leads to increasing *LFW*. Fig. 2d – f shows the characteristic moment – folding angle curves depending on the number of folding cycles for the respective hinge classes: Aramid hinges and photopolymer hinges show a pronounced decrease of the slope, while the accumulation of plastic deformation prevails for PA hinges. The darkest color represents the first folding cycles. The number of folding cycles increases with brightness of the color of the curves, up to 10^6 cycles for aramid and PA hinges and 10^4 cycles for the photopolymer hinge (marked red).

The *ULL* and *LFW* show a decrease with increasing numbers of folding cycles, which can be attributed to fatigue (Fig. 2g). The top graph shows the *ULL* normalized by the as-printed properties (round data points) and the failure probability (square data points) of the hinges versus the number of folding cycles. The *LFW* normalized by the as-printed properties is shown in the bottom graph. A decreasing trend for all hinge classes is found. When comparing the *LFW* and the residual angle with the theoretical model of constant stiffness, a reduction in stiffness can be observed for the aramid and photopolymer hinges, while the stiffness of the PA hinges does not change greatly (Fig. 2i). In spite of the viscoelastic material properties, we do not observe a significant effect of the strain rate on the fatigue, which would appear as a discontinuity in the data from 200 to 1000 folding cycles.

The micrographs of the SEM investigation are depicted in Fig. 3. The first column shows the as-printed hinges, while the other columns show specimens after cyclic fatigue. Two fatigue mechanisms are found in the aramid hinges, fiber buckling leading to matrix rupture on the compression side (Fig. 3a-II, III), and fiber rupture on the tensile side (Fig. 3a-IV). First signs of crack nucleation are observed on the surface of the PA hinge after 10^6 cycles (Fig. 3b-II). The fracture surface of a PA specimen that failed after 10^6 cycles is shown in Fig. 3b-V, VI. The photopolymer hinges exhibit cracks after 10^3 folding cycle, which propagate across the hinge width and thickness until a complete fracture (Fig. 3c).

The results of the different experiments are combined in Fig. 4. The *LFW* is plotted against the *ULL* for the three hinge classes. The grey shaded zones indicate the change in properties due to fatigue. The length of the shadow provides information about the extent of fatigue and greyscale the number of the elapsed folding cycles. The dashed lines illustrate the change in properties resulting from a change in the respective design parameter.

4. Discussion

4.1. Influence of design parameters on mechanical properties

The mechanical properties of the hinge can be tailored by the design parameters (Fig. 2a-c). The ultimate line load (*ULL*) of the hinges strongly depends on the amount of material in the hinge region. The experimental results shown in Fig. 2a-c (top row) indicate a linear relationship between the *ULL* and both the number of fiber bundles, and the thickness of the hinge. For the aramid hinges, an increase in load carrying capability of 50 N per aramid fiber bundle is found. This corresponds to a nominal tensile strength of 408 MPa, which is well below the 610 MPa reported by the supplier [21]. This discrepancy can be explained by the fact that not all fibers are carrying the same amount of load. The fibers at the bottom side of the hinge sag downwards, due to a lack of support while printing (Fig. 3a-I). Therefore, not all fibers are loaded equally under the uniaxial tension. This could be improved by the introduction of supports for printing the fibers across the hinge gap. However, the removal of these supports could lead to surface imperfections. Especially under flexural loading, this would lead to stress concentrations. The nominal tensile strength of the polyamide (PA) hinges has been found to be 43.4 MPa for a thickness of 0.2 mm and 47.4 MPa for a thickness of 0.1 mm. Literature suggests a slightly higher value of approximately 54 MPa [22]. This discrepancy originates from local stress concentrations near the interface to rigid segments, due to the asymmetric design of the hinge. This is also the region, where failure is observed in the tensile tests. The maximum stress at the interface between the rigid segments and the hinge region is considerably higher than the nominal stress calculated. A brief examination of the stress concertation in the PA hinges by means of finite element simulation

Fig. 2. Mechanical properties of the different hinge classes. (a-c) The ultimate line load (ULL) (top row) and line folding work (LFW) (bottom row) depend strongly on the design parameters number of fiber bundles and hinge thickness. (d-f) The different hinges show varying hysteresis loops, which change significantly with an increasing number of folding cycles. (g) Fatigue can be quantified by investigating the decrease of ULL and LFW depending on the cyclic deformation. (h) The theoretical model of constant elastic properties can be applied to determine the source of LFW decay. (i) The experimental data applied to the theoretical model indicates a stiffness reduction for PA and photopolymer hinges and a constant stiffness for the PA hinges. (For interpretation of the references to color in this figure, the reader is referred to the web version of this article.)

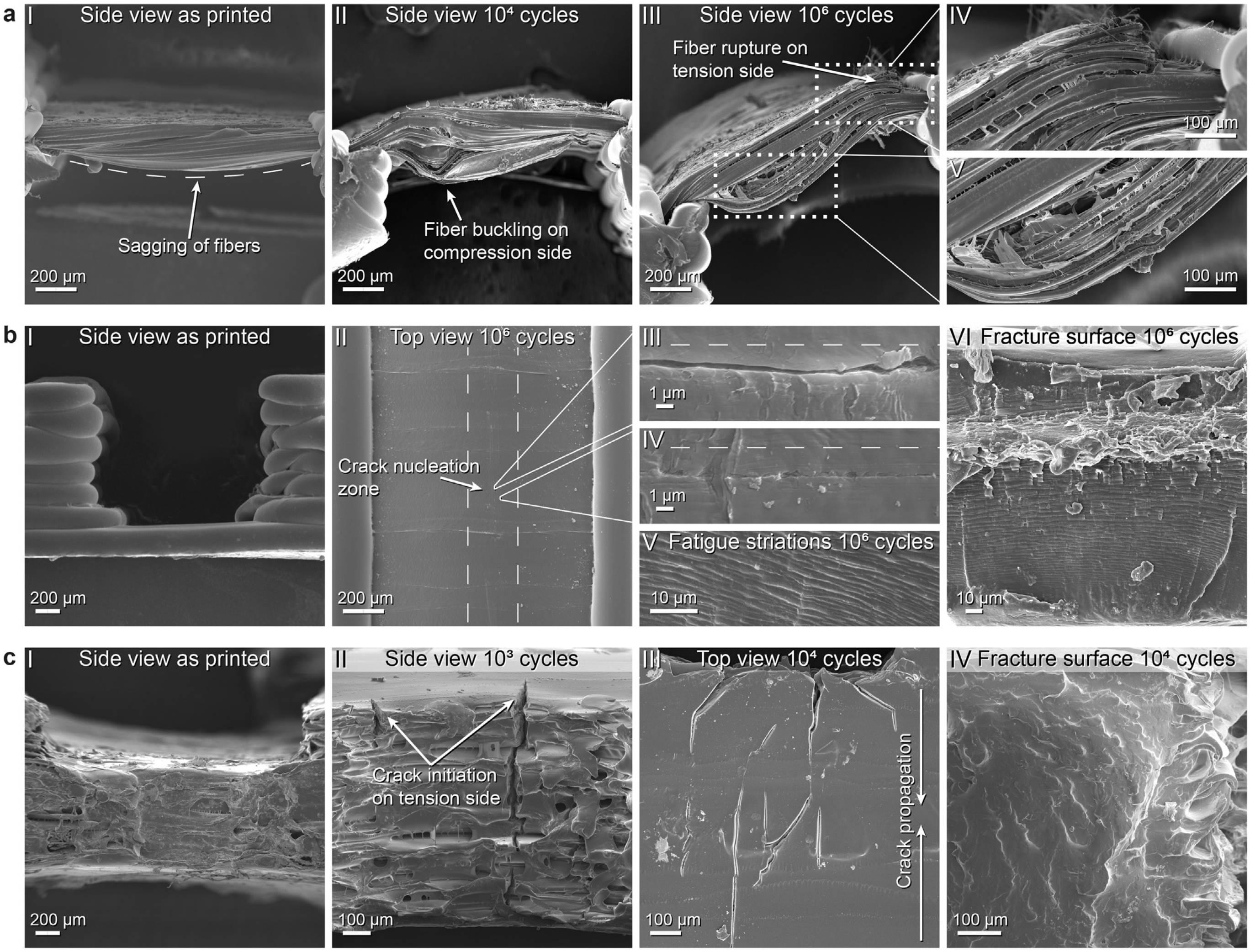
a
I Side view as printed
Sagging of fibers
200 μm
II Side view 10⁴ cycles
Fiber buckling on compression side
200 μm
III Side view 10⁶ cycles
Fiber rupture on tension side
200 μm
IV
100 μm
V
100 μm
b
I Side view as printed
200 μm
II Top view 10⁶ cycles
Crack nucleation zone
200 μm
III
1 μm
IV
1 μm
V Fatigue striations 10⁶ cycles
10 μm
VI Fracture surface 10⁶ cycles
10 μm
c
I Side view as printed
200 μm
II Side view 10³ cycles
Crack initiation on tension side
100 μm
III Top view 10⁴ cycles
Crack propagation
100 μm
IV Fracture surface 10⁴ cycles
100 μm

Fig. 3. SEM micrographs of aramid hinges (a), PA hinges (b) and photopolymer hinges (c). Aramid hinges fatigue by fiber buckling under compression resulting in matrix rupture (a-II and a-V) and fiber rupture under tensile loading at cycle numbers above 10^4 cycles (a-IV). The fatigue of PA hinges depends strongly on the conditioning and surface quality. Some specimens exhibit first crack nucleation sites after 10^6 folding cycles (b-II – IV), others fractured completely (b-V, VI). The photopolymer hinges show fatigue cracks after 10^3 cycles initiating from regions with the highest tensile stress (c-II). These cracks propagate across the complete width (c-III).

can be found in the SI. The photopolymer hinges show an average nominal tensile strength of 2.4 MPa. This value coincides with the 2.4–3.1 MPa reported by the supplier [24]. The hinges failed inside the flexible polymer, not at the interface between the rigid and the flexible photopolymer, which is in accordance with literature [30].

The work required for folding the hinge strongly depends on both the number of fiber bundles and the hinge thickness (Fig. 2a-c bottom row). While this finding coincides with expectation, the influence of the hinge length appears to be counterintuitive at the first glance. The line folding work (*LFW*) of PA and photopolymer hinges decreases with the increase in the hinge length. This finding is in accordance with intuition, since longer hinge areas lead to lower strains, stresses and thus a lower *LFW*. For the aramid hinges however, the opposite trend can be observed. An increase in hinge length leads to an increase in *LFW*. This alleged inconsistency can be explained by looking at the local deformation in the material for the respective hinges. The PA and photopolymer hinges exhibit a continuous strain distribution throughout the whole length of the bent segment. In contrast to that, the aramid hinges deform predominantly at a localized spot close to the rigid segment. In this region, the thickness of the aramid fiber bundle is lower than in the center of the hinge (Fig. 3a-I). The strain in the fibers exceeds the elastic limit and plastic hinging occurs at the location with the lowest resistance, e.g. the reduced thickness region. Naturally, fiber composites exhibit a much higher stiffness under tensile loading than in compression. This stiffness disparity leads to a shift of the neutral axis towards the tension side. Compression of the fibers accommodates most of the deformation. The compressive stress results in buckling of the fibers, causing large deformation and inter-fiber failure of the PA matrix (Fig. 3a-I, II). For increasing hinge lengths, the stress and strain due to fiber buckling on the compression side is distributed to a larger volume of matrix material and thus the *LFW* increases.

The mechanical properties for the different classes of hinges span an enormous range. Both the *ULL* and the *LFW* vary by almost one and a half orders of magnitude. Further, the properties can be tailored precisely by careful design of the hinge. The composite hinge greatly outperforms both PA and photopolymer hinges in terms of maximum achievable *ULL* in the as-printed state. Its tensile and flexural properties are highly controllable by the design of the hinge region.

4.2. Fatigue mechanisms and their impact on mechanical properties

The fatigue of the flexural hinges is studied by analyzing changes in *ULL* and *LFW*, by investigation of the characteristic bending moment – folding angle, and by inspection using SEM. The combination of the findings from these three approaches allows the inference of the fatigue mechanisms.

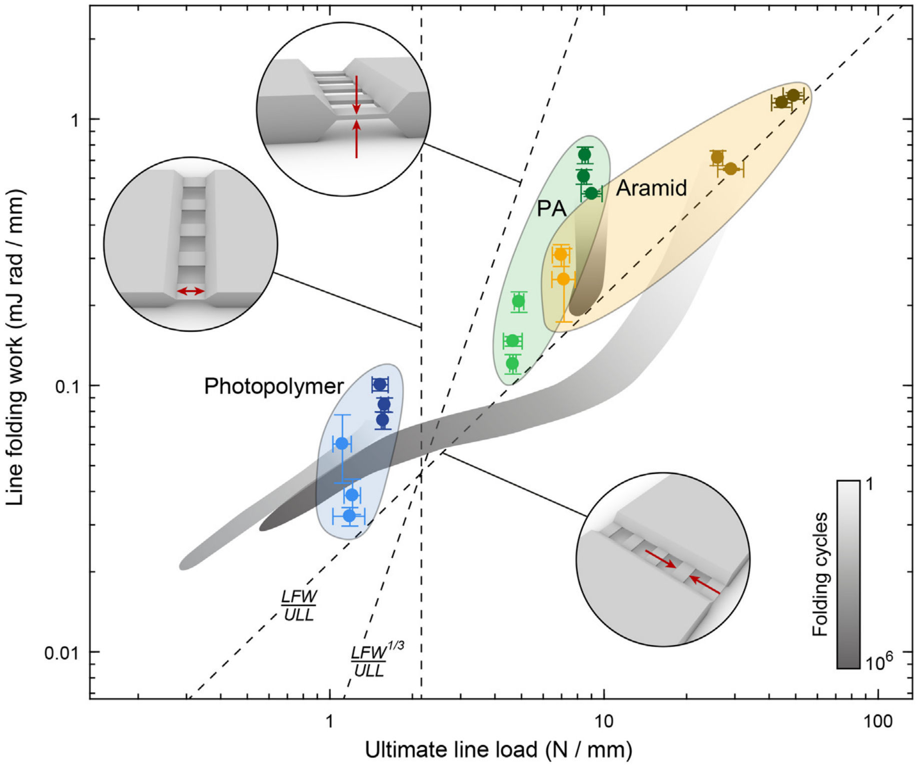

Fig. 4. Property map comparing ultimate line load (ULL) and line folding work (LFW) of the different hinge classes. Fatigue is indicated as grey shadows. The greyscale provides information about the number of folding cycles. The dashed lines mark the change in ULL and LFW due to variation of the respective design parameter. Large regions of the property space can be accessed by materials selection and optimization of the design parameters. Modifying the hinge thickness leads to changing LFW while the ULL remains unaffected (vertical dashed line). A change in the amount of material in the hinge region with constant thickness leads to a linear scaling of both ULL and LFW. Thus, the properties change along the dashed line with slope one. Tuning the hinge thickness results in a linear change in ULL and the LFW changes with the power of three. The dashed line with slope three illustrates this scaling.

The aramid hinges show an increase in *ULL* between 200 and 1000 folding cycles (Fig. 2 g). This most likely originates from the different folding procedures. The samples up to 200 folding cycles are folded manually, whereas the other samples are folded on the Hydropuls fatigue testing setup. From the jump in the data, it can be concluded that manual folding leads to a more rapid decrease in ULL, most likely because of slight variations in the folding axis.

Both the *ULL* and the *LFW* of the aramid hinges show a strong decrease with an increasing number of folding cycles. Starting from the first cycle, a stiffness decrease in the hysteresis loops can be observed (Fig. 2d). Similarly, the strong deviation from the theoretical model of constant stiffness indicates a stiffness decreasing fatigue mechanism in the aramid hinges (Fig. 2i). This originates from the deformation mode of the fiber bundles upon folding, which is examined in the previous section. Fiber buckling under compression results in high tensile stresses in the PA matrix. This leads to excessive plastic deformation and formation of inter-fiber cavities in the matrix (Fig. 3a-II, III, V). Upon unfolding, the cavities close and the resistance of the cavity walls under compressive stress conditions is small. The variation in deformation mechanism for tension and compression results in an enormous hysteresis, which can be observed most significantly in the initial folding cycles. With increasing number of cycles, an interconnected network of voids between the aramid fibers forms, due to breaking of the PA matrix (Fig. 3a-IV, V). Consequently, the resistance to folding decreases strongly (Fig. 2d). Moreover, the *ULL* is affected by this fatigue mechanism. With increasing plastic deformation, the load distribution in the fibers becomes progressively inhomogeneous under tensile loading conditions, lowering the *ULL*. Besides failure of the PA matrix, fiber fracture in the region maximum tensile stress (Fig. 3a-III, IV) is observed. The fiber ruptures at a later stage of the fatigue life than the fiber buckling. After folding the aramid hinge for 10^4 times, no indication of fiber rupture is present, whereas the sample after 10^6 folding cycles exhibits large quantities of ruptured fibers. This is the fatigue mechanism, which eventually results in failure of the hinge. Overall, the aramid hinges show low resistance to fatigue. There is no stable regime and constant reduction of *ULL* and *LFW* prevail. The enormous hysteresis loop in the early folding cycles makes the aramid hinges uniquely suited for energy absorption applications.

The fatigue behavior of the PA hinges deviates strongly from the one discussed previously. The *ULL* is stable up 10^4 folding cycles (Fig. 2g). Subsequently, only a slight decrease in the *ULL* can be observed. The *LFW* shows a decreasing trend. However, the reduction in *LFW* can be attributed to the accumulation of plastic deformation, lowering the effective folding angle (Fig. 2i) rather than to a reduction of the hinge stiffness. The very onset of crack nucleation is observed on the surface of the hinge specimen after 10^6 folding cycles (Fig. 3b-III, IV, the dashed line indicates the orientation on the hinge region). Parallel surface cracks are visible perpendicular to the tensile stresses on the surface, spanning a width of only 50–500 Nm. These imperfections form in the center of the hinge region at the location of maximum tensile stress. The scission and relative sliding of single molecular chains lead to the formation of nucleation sites on the surface [31]. Hence, a multi-axial stress-state develops and the material yields locally (rough surface features in Fig. 3b-III, IV). These steps amplify the local stress concentration, resulting in a self-catalyzing propagation of the surface crack perpendicular to the tensile stress in plane and through the thickness of the hinge (Fig. 3b-III). This marks the transition from the cyclic stable stage of the fatigue life to the crack initiation stage. At this point, the mechanical properties are not yet affected significantly. Under further cyclic loading, the cracks will propagate deeper into the material and start to coalesce. The onset of fatigue crack initiation in PA depends strongly on the environmental conditions, e.g. absorbed humidity from the air acting as plasticizer. While the specimen depicted in

Fig. 3b-II exhibits only first signs of a fatigue crack, other samples showed failure after 10^6 cycles.

The fatigue fracture surface of a failed specimen is displayed in Fig. 3b-VI. During initial folding, the top side of the fracture surface was loaded in tension and the bottom side in compression. As the crack initiates at the top and propagates through the thickness of the hinge, the neutral axis and hence the tensile and compression region shift downwards. Characteristic fatigue striations, which originate from consecutive crack arrest and growth, can be found on large portion of the surface. Other than in metals each line does not necessarily correspond to a single cycle of loading [32]. The width of the bands decreases towards the lower side of the fracture surface. Under the assumption that the crack initiates at the top tensile sides and propagated through the thickness, the change in the width of the bands can be explained by the reduction of the peak stress, as the effective thickness gets smaller. In the upper half of the fracture surface, a large feature of yielded material can be found, spanning across the complete width of the hinge. Ledges are visible, which form when cracks originating from different planes, approach one another and coalesce. PA is known for its good fatigue properties with a life of up to several million cycles [33]. In this study, PA hinges exhibit stable properties up to 10^5 folding cycles. After that, the crack initiation and cyclic growth might begin depending on the conditioning of the specimens. Under the right conditions (e.g. sufficiently high humidity), the hinges can withstand 10^6 folding cycles without deterioration of their mechanical properties.

The photopolymer hinges exhibit the lowest resistance to fatigue. A decrease in *ULL* beginning already at 100 folding cycles can be observed. Since the elastomeric photopolymer consists of a cross-linked network, there is essentially no plastic deformation (Fig. 2f). The residual folding angle remains zero up to the point of failure. The photopolymer has the interesting property that the two surfaces of a crack adhere to each other when the crack is closed. After closure of the crack during unfolding, a significant amount of stress can be carried across the adhering crack surfaces. If the stress is sufficiently high, the crack opens and the stiffness drops. This explains why the moment at low folding angles changes less than the moment at folding angles above 70°.

The side surface of the photopolymer hinges appears very rough and irregular (Fig. 3 c-I, II). This can originate either from the printing process, or from the cleaning procedure, which was applied to the specimens before SEM imaging. The residues of the hydrogel support material on the specimen surface is dissolved chemically by immersion in a solution of 2 vol% sodium hydroxide and 1 vol% sodium silicate for 5 h (as suggested by the supplier [25]). It is unclear to which extent this procedure affects the surface of the photopolymer. Cracks are exclusively found on hinges, which have been subjected to fatigue testing. Thus, they should not originate from the cleaning procedure. After 10^{3} cycles, cracks are visible initiating from sites of stress concentrations, where the tensile stress and the stress caused by the Poisson effect superimpose (Fig. 3c-II). With increasing cyclic deformation, the cracks propagate through the thickness direction as well as in plane. Cracks initiate at different locations grow and approach. Thus, the loading conditions change, resulting in the formation of bifurcations and alternating propagation directions (Fig. 3c-III). This proceeds until the cracks coalesce, forming an interconnected network across the hinge width, significantly weakening the hinge and ultimately resulting in failure. The fracture surface after 10^4 folding cycles exhibits no signs of fatigue striations (Fig. 3c-IV). The overall morphology of the surface appears rough with marks similar to ledges. These features originate from changes in propagation direction and coalescence of cracks. The photopolymer hinges exhibit an accelerated decay of the *ULL* and *LFW* after 100 folding cycles (Fig. 2g), which can be attributed to the formation and propagation of cracks.

The investigated hinges behave fundamentally differently when subjected to cyclic deformation. The aramid hinges and the photopolymer hinges show limited resistance to fatigue. Most of the fatigue life is spent in crack propagation, which results in steadily decreasing mechanical properties. This is a characteristic of low cycle fatigue [34]. The PA hinges in contrast exhibits crack initiation and growth at a much higher number of folding cycles, indicating a high cycle fatigue behavior.

In general it can be observed, that a drop in *ULL* is always accompanied by the reduction in the bending stiffness and hence the *LFW*. This relation offers the opportunity to develop a smart hinge concept, in which the *LFW* is monitored to predict the residual *ULL* of the hinge and prevent failure in duty. This concept will be addressed in the future studies.

4.3. A guideline for the design of flexural hinges

All the experimental data is condensed into a double logarithmic representation of the *ULL* and *LFW* (Fig. 4). This graph enables the comparison of the achievable properties for the different classes of hinges. Thus, it provides a tool to select the material and design parameter based on the target properties of the hinge. The change in mechanical properties due to fatigue is illustrated as grey shadows. The greyscale indicates the number of folding cycles. The shorter and darker the shadow, the higher if the resistance to fatigue of the hinge. The dashed lines represent the scaling of the mechanical properties depending on the change of the respective design parameter. If the hinge length is changed, the *LFW* can be tuned while the *ULL* remains unaffected. Thus, we move along the vertical dashed line. A change in the amount of material in the hinge with constant thickness, as it is the case for the different numbers of fiber bundles of the aramid hinges, results in a linear scaling of both the *ULL* and the *LFW* (dashed line with slope 1). An increase in thickness, as for the PA and the photopolymer hinges, leads to a linear scaling of the ULL, while the *LFW* scales with the power of three (dashed line with slope 1/3).

Even though the linearized beam equations are generally not valid for structures undergoing large deformations, the observed relationship suggests that the stiffness of the PA and photopolymer hinges can be described by the analytical equations of the bending beam. Hence, the hinge can be modeled with a bending stiffness:

$$k_b = \frac{EI}{L} \tag{2}$$

with

$$I = \frac{b\,t^3}{12} \tag{3}$$

k_b represents the bending stiffness, E is Young's modulus and I is the area moment of inertia of a bending beam with rectangular cross section, L is the length of the hinge, b is the width of the hinge, and t is the thickness. The work required for folding the hinge is directly related to the bending stiffness of the hinge by:

$$W_f = \frac{1}{2}\,k_b\,\alpha^2 = \frac{E\,b\,t^3}{24\,L}\,\alpha^2 \tag{4}$$

with the folding angle α. This equation applies to the dashed lines in Fig. 4 for scaling of the design parameters hinge width b, length L and thickness t.

When tuning the individual design parameters, the *ULL* and *LFW* change along linearly independent vectors in the 2D property space. Therefore, the *ULL* and *LFW* can be decoupled when designing the hinge. This is only valid for a certain range of values, set by physical limitations, e.g. at a certain hinge thickness the strain during folding will exceed the failure strain of the material.

Fig. 4's property map implies that the selection of the hinge material depends on the requirements set by the application. The aramid hinges are the first choice for high loading scenarios with low numbers of folding. PA hinges show the best performance over elevated numbers of cyclic deformation, and the photopolymer hinges exhibit the lowest resistance to folding, which allows the use of low-power actuators.

5. Conclusion

In this work, we contribute to the field of 3D-printed origami-inspired structures in three respects. First, the concept of an aramid fiber composite hinge is introduced, which can be fabricated by multimaterial fused deposition modeling (FDM) printing. Second, the dependence of the design parameters on the mechanical properties of hinges is studied. And third, the fatigue behavior and underlying mechanisms of the respective hinge classes is characterized. The aramid hinge shows an exceptionally high ultimate line load (*ULL*), outperforming the other two hinge classes investigated. However, the resistance to fatigue is very low, which originates from the deformation mode of the composite. The fatigue mechanisms acting in the respective materials are identified. These mechanisms differ greatly between the materials, leading to fundamentally different fatigue behaviors. While the resistance to fatigue is low for the aramid and the photopolymer hinges, polyamide (PA) hinges exhibit no significant reduction of mechanical properties up to 10^6 folding cycles. A framework is provided, which enables the comparison of the mechanical properties as a function of design parameters and fatigue of the different hinge classes. Hence, it serves as a tool for material selection and as a guideline for the design of flexural hinges. With the presented work, we hope to provide a foundation to bring 3D-printed origami-inspired structures closer to real world applications. To achieve this, a thorough understanding of the mechanical properties and the fatigue behavior is a basic prerequisite.

CRediT authorship contribution statement

Marius A. Wagner: Conceptualization, Investigation, Formal analysis, Writing - original draft, Writing - review & editing. **Jian-Lin Huang:** Investigation, Formal analysis, Writing - review & editing. **Philipp Okle:** Conceptualization, Investigation, Formal analysis. **Jamie Paik:** Conceptualization, Writing - review & editing. **Ralph Spolenak:** Conceptualization, Writing - review & editing, Supervision.

Declaration of competing interest

The authors declare that they have no known competing financial interests or personal relationships that could have appeared to influence the work reported in this paper.

Acknowledgements

The authors acknowledge the support of the contributors who have made this work possible. Dominic Keidel helped to perform the fatigue tests. Till Kyburz and Christian Wegmann fabricated parts of the experimental setup. Hassan Baysal helped to perform experimental characterization and specimens fabrication. Qin Xu contributed to the characterization of the flexural properties. Jung-Chew Tse contributed by fabrication of specimens. Prof. Kristina Shea, Prof. Paolo Ermanni and Prof. Eric Dufresne provided access to their laboratory facilities and equipment. The authors also acknowledge support of the Scientific Center for Optical and Electron Microscopy (ScopeM) of the Swiss Federal Institute of Technology Zurich ETHZ. This study is part of the strategic focus area advanced manufacturing project Sustainable Design of 4D Printed Active Systems (SD4D).

Data availability

The raw/processed data required to reproduce these findings cannot be shared at this time due to technical or time limitations. Data is available upon request.

Appendix. Supplementary data

Supplementary data to this article can be found online at https://doi.org/10.1016/j.matdes.2020.108643.

References

[1] P. Hunter, Nature's origami, EMBO Rep. 16 (11) (2015) 1435–1438.
[2] F. Haas, S. Gorb, R. Wootton, Elastic joints in dermapteran hind wings: materials and wing folding, Arthropod structure & development 29 (2) (2000) 137–146.
[3] R.J. Lang, From Flapping Birds to Space Telescopes: The Modern Science of Origami, NPAR, 2008.
[4] L. Wilson, S. Pellegrino, R. Danner, Origami sunshield concepts for space telescopes, 54th AIAA/ASME/ASCE/AHS/ASC Structures, Structural Dynamics, and Materials Conference, 2013.
[5] J.T. Overvelde, et al., Rational design of reconfigurable prismatic architected materials, Nature 541 (7637) (2017) 347.
[6] T. Chen, et al., Autonomous deployment of a solar panel using elastic origami and distributed shape-memory-polymer actuators, Physical Review Applied 11 (6) (2019) 64069.
[7] H. Yasuda, J. Yang, Reentrant origami-based metamaterials with negative Poisson's ratio and bistability, Phys. Rev. Lett. 114 (18) (2015) 185502.
[8] J.A. Faber, A.F. Arrieta, A.R. Studart, Bioinspired spring origami, Science 359 (6382) (2018) 1386–1391.
[9] J.L. Silverberg, et al., Origami structures with a critical transition to bistability arising from hidden degrees of freedom, Nat. Mater. 14 (4) (2015) 389.
[10] E. Boatti, N. Vasios, K. Bertoldi, Origami metamaterials for tunable thermal expansion, Adv. Mater. 29 (26) (2017) 1700360.
[11] J.L. Silverberg, et al., Using origami design principles to fold reprogrammable mechanical metamaterials, science 345 (6197) (2014) 647–650.
[12] A. Firouzeh, J. Paik, Robogami: a fully integrated low-profile robotic origami, Journal of Mechanisms and Robotics 7 (2) (2015) 21009.
[13] Z. Zhakypov, et al., Designing minimal and scalable insect-inspired multi-locomotion millirobots, Nature 571 (7765) (2019) 381–386.
[14] S. Miyashita, et al., Robotic metamorphosis by origami exoskeletons, Science Robotics 2 (10) (2017) eaao4369.
[15] S. Felton, et al., A method for building self-folding machines, Science 345 (6197) (2014) 644–646.
[16] B.G. Winder, S.P. Magleby, L.L. Howell, A study of joints suitable for lamina emergent mechanisms, ASME 2008 International Design Engineering Technical Conferences and Computers and Information in Engineering Conference, American Society of Mechanical Engineers Digital Collection, 2009.
[17] L.L. Howell, Compliant Mechanisms, John Wiley & Sons, 2001.
[18] I.L. Delimont, S.P. Magleby, L.L. Howell, Evaluating compliant hinge geometries for origami-inspired mechanisms, Journal of Mechanisms and Robotics 7 (1) (2015) 011009.
[19] Z. Zhao, et al., 3D printing of complex origami assemblages for reconfigurable structures, Soft Matter 14 (39) (2018) 8051–8059.
[20] I. Gibson, et al., Design rules for additive manufacture, Solid Freeform Fabrication Symposium, University Of Texas Austin, TX, 2010.
[21] Markforged Composite Material Datasheet, [cited 2019 September]; Available from https://static.markforged.com/markforged_composites_datasheet.pdf 2019.
[22] Markforged material datasheet Though Nylon, [cited 2019 September]; Available from https://support.markforged.com/hc/en-us/articles/209934406-Tough-Nylon 2019.
[23] Stratasys VeroWhitePlus material datasheet 2019 [cited 2019 September]; Available from: https://support.stratasys.com/materials/polyjet-materials/vero-family-(rigid).
[24] Stratasys Agilus30 material datasheet, [cited 2019 September]; Available from https://www.stratasys.com/de/materials/search/agilus30 2019.
[25] Stratasys Bio-Compatibility Requirements2019 (cited 2019 September]; DOC-08381 Rev. D).
[26] D. Blanco, P. Fernandez, A. Noriega, Nonisotropic experimental characterization of the relaxation modulus for PolyJet manufactured parts, J. Mater. Res. 29 (17) (2014) 1876–1882.
[27] T. Elder, D. Rozairo, A.B. Croll, Origami inspired mechanics: measuring modulus and force recovery with bent polymer films, Macromolecules 52 (2) (2019) 690–699.
[28] M. Wagner, T. Chen, K. Shea, Large shape transforming 4D auxetic structures, 3D Printing and Additive Manufacturing 4 (3) (2017) 133–142.
[29] Z. Zhakypov, J.-L. Huang, J. Paik, A novel torsional shape memory alloy actuator: modeling, characterization, and control, IEEE Robotics & Automation Magazine 23 (3) (2016) 65–74.
[30] T.S. Lumpe, J. Mueller, K. Shea, Tensile properties of multi-material interfaces in 3D printed parts, Mater. Des. 162 (2019) 1–9.
[31] J. Rösler, H. Harders, M. Baeker, Mechanical Behaviour of Engineering Materials: Metals, Ceramics, Polymers, and Composites, Springer Science & Business Media, 2007.
[32] M. Hayes, D. Edwards, A. Shah, Fractography in Failure Analysis of Polymers, William Andrew, 2015.
[33] L.W. McKeen, Fatigue and Tribological Properties of Plastics and Elastomers, William Andrew, 2016.
[34] P. Beardmore, S. Rabinowitz, Fatigue Deformation in Polymers, Academic Press, New York, 1975.